

20-12-2005

## Reflections of Active Galactic Nucleus Outbursts in the Gaseous Atmosphere of M87

W. Forman

*Harvard-Smithsonian Center for Astrophysics, Cambridge, USA*

P. Nulsen

*University of Wollongong*

S. Heinz

*Massachusetts Institute of Technology, USA*

F. Owen

*National Radio Astronomy Observatory, Socorro, USA*

J. Eilek

*New Mexico Tech, Socorro, USA*

*See next page for additional authors*

Follow this and additional works at: <https://ro.uow.edu.au/engpapers>



Part of the [Engineering Commons](#)

<https://ro.uow.edu.au/engpapers/293>

---

### Recommended Citation

Forman, W.; Nulsen, P.; Heinz, S.; Owen, F.; Eilek, J.; Vikhlinin, A.; Markevitch, M.; Kraft, R.; Churazov, E.; and Jones, C.: Reflections of Active Galactic Nucleus Outbursts in the Gaseous Atmosphere of M87 2005.  
<https://ro.uow.edu.au/engpapers/293>

---

**Authors**

W. Forman, P. Nulsen, S. Heinz, F. Owen, J. Eilek, A. Vikhlinin, M. Markevitch, R. Kraft, E. Churazov, and C. Jones

## REFLECTIONS OF ACTIVE GALACTIC NUCLEUS OUTBURSTS IN THE GASEOUS ATMOSPHERE OF M87

W. FORMAN,<sup>1</sup> P. NULSEN,<sup>1,2</sup> S. HEINZ,<sup>3</sup> F. OWEN,<sup>4</sup> J. EILEK,<sup>5</sup> A. VIKHLININ,<sup>1,6</sup>  
 M. MARKEVITCH,<sup>1</sup> R. KRAFT,<sup>1</sup> E. CHURAZOV,<sup>6,7</sup> AND C. JONES<sup>1</sup>

Received 2003 December 21; accepted 2004 October 22

### ABSTRACT

We combined deep *Chandra*, *ROSAT* HRI, and *XMM-Newton* observations of M87 to study the impact of active galactic nucleus (AGN) outbursts on its gaseous atmosphere. Many X-ray features appear to be a direct result of repetitive AGN outbursts. In particular, the X-ray cavities around the jet and counterjet are likely due to the expansion of radio plasma, while rings of enhanced emission at 14 and 17 kpc are probably shock fronts associated with outbursts that began  $1\text{--}2 \times 10^7$  yr ago. The effects of these shocks are also seen in brightenings within the prominent X-ray arms. On larger scales,  $\sim 50$  kpc from the nucleus, depressions in the surface brightness may be remnants of earlier outbursts. As suggested for the Perseus Cluster by Fabian and his coauthors, our analysis of the energetics of the M87 outbursts argues that shocks may be the most significant channel for AGN energy input into the cooling-flow atmospheres of galaxies, groups, and clusters. For M87, the mean power driving the shock outburst,  $2.4 \times 10^{43}$  ergs s<sup>−1</sup>, is 3 times greater than the radiative losses from the entire cooling flow. Thus, even in the absence of other energy inputs, outbursts every  $3 \times 10^7$  yr are sufficient to quench the flow.

**Subject headings:** galaxies: active — galaxies: individual (M87, NGC 4486) — X-rays: galaxies

### 1. INTRODUCTION

M87 (NGC 4486) provides a unique laboratory in which to study the interaction between energy generated by a supermassive black hole and the hot intracluster medium. Its proximity allowed the disk surrounding its active nucleus to be resolved by the *Hubble Space Telescope* (*HST*), providing a measure for the mass of the central black hole of  $3.2 \times 10^9 M_\odot$  (Harms et al. 1994; Ford et al. 1994; Macchetto et al. 1997). M87’s proximity also provides a unique view of its jet, detected in optical, X-ray, and radio (e.g., Sparks et al. 1996; Perlman et al. 2001; Marshall et al. 2002; Harris et al. 2003).

M87 is the central elliptical galaxy in the rich Virgo Cluster and is surrounded by an extensive gaseous atmosphere with a mean temperature of  $\sim 2\text{--}2.5$  keV (Mathews 1978; Bahcall & Sarazin 1977; Fabricant & Gorenstein 1983; Böhringer et al. 2001; Matsushita et al. 2002). X-ray structure in the gaseous halo of M87 was first reported by Feigelson et al. (1987) using *Einstein Observatory* observations. Using *ROSAT* and *XMM-Newton* observations, Böhringer et al. (1995), Churazov et al. (2001), and Belsole et al. (2001) discussed the relationship between the observed X-ray structure and the radio emission.

Like many other optically luminous galaxies at the centers of clusters, M87 has been considered to be a classic example of a cooling-flow system, in which the gas cooling time is relatively short compared to the age of the system (e.g., Stewart et al. 1984;

Nulsen & Böhringer 1995; Böhringer et al. 2001). However, observations with *XMM-Newton* have shown that cooling flows, such as that around M87, deposit cooled gas at much lower rates than expected in the standard cooling-flow model (Fabian 1994; Peterson et al. 2003 and references therein). This requires considerable energy input to compensate for radiative losses. M87, with its proximity, its active nucleus, jet, and extensive system of radio lobes, provides an ideal system for studying the energy input from the active galactic nucleus (AGN) to the hot, cooling gas.

Using radio studies, Owen et al. (2000; see also Binney 1999) pioneered the view that the mechanical power produced by the supermassive black hole at the center of M87 was more than sufficient to compensate for the energy radiated in X-rays. Tabor & Binney (1993) and Binney & Tabor (1995) developed models without mass deposition and included energy injection from the central AGN. Heinz et al. (1998; see also Reynolds et al. 2001) modeled shock heating of the intracluster medium (ICM) by an expanding radio source. Churazov et al. (2001; see also Kaiser & Binney 2003; Bruggen 2003; De Young 2003; Kaiser 2003) first argued that the morphology of the X-ray and radio observations could be explained by radio-emitting plasma bubbles buoyantly rising through the hot X-ray-emitting gas. Furthermore, Churazov et al. showed that these buoyant bubbles could uplift the coolest gas and provide significant energy input as bubble enthalpy is converted to kinetic energy, then thermalized into the gas in the bubble wake.

The results outlined above relied primarily on pre-*Chandra* observations of M87 that lacked sufficient angular resolution to allow detailed comparison to the radio structures shown in the Owen et al. (2000) study. Young et al. (2002) used a 37 ks *Chandra* observation to both confirm previous structures and describe several new features, including two nearly spherical “edges” at  $\sim 45''$  and  $\sim 3'$ , which they attribute to activity in the nucleus associated with jet production. The *Chandra* images also show cavities and filaments in the eastern and southwestern X-ray arms. Young et al. argued that the arms were overpressurized and multitemperature. Molendi (2002) used *XMM-Newton* observations to show that the

<sup>1</sup> Smithsonian Astrophysical Observatory, Harvard-Smithsonian Center for Astrophysics, 60 Garden Street, Cambridge, MA 02138; wrf@cfa.harvard.edu.

<sup>2</sup> On leave from the University of Wollongong.

<sup>3</sup> Massachusetts Institute of Technology, 77 Massachusetts Avenue, Cambridge, MA 02139-4307.

<sup>4</sup> National Radio Astronomy Observatory, P.O. Box O, Socorro, NM 87801.

<sup>5</sup> Department of Physics, New Mexico Tech, 801 Leroy Place, Socorro, NM 87801.

<sup>6</sup> Space Research Institute (IKI), Profsoyuznaya 84/32, Moscow 117810, Russia.

<sup>7</sup> Max-Planck-Institut für Astrophysik, Karl-Schwarzschild-Strasse 1, 85740 Garching, Germany.

X-ray arms required two-temperature models with gas temperatures in the ranges  $kT \sim 0.8\text{--}1$  keV and  $kT \sim 1.6\text{--}2.5$  keV.

In this paper, we combine deep *Chandra*, *ROSAT* HRI, and *XMM-Newton* observations to study the impact of AGN outbursts on the gaseous atmosphere around M87 and the interaction of the radio-emitting plasma with the hot gas. As others have noted, the *Chandra*, *XMM-Newton*, and *ROSAT* HRI observations show rich structure on many angular scales. These include knots in the jet, surrounding cavities, a coincident X-ray and radio bubble just budding from the southeast of the radio core region, a weak shock, filaments and cavities in the east and southwest arms, and an arclike region of enhanced emission coincident with the outer edge of the southern radio halo. In this paper, we describe the X-ray observations and discuss the origin of these features in M87.

## 2. OBSERVATIONAL DETAILS

M87 has been well studied at all wavelengths and by each new X-ray mission. Here, we describe our analysis for *Chandra*, *XMM-Newton*, and the *ROSAT* HRI. X-ray observations were obtained from the *Chandra*, *XMM-Newton*, or HEASARC archives. While *Chandra* provides unprecedented angular resolution, *XMM-Newton* and the *ROSAT* HRI yield large field of view (FOV) images with which to study the larger scale structures around M87. We adopt a distance for M87 of 16 Mpc (Tonry et al. 2001), which yields a scale of  $4.65$  kpc arcmin<sup>-1</sup>. We used a broad suite of tools to analyze the *ROSAT*, *Chandra*, and *XMM-Newton* data, including XSPEC 11.2.0, FTOOLS, CIAO 3.0.1, and SAS 5.3. All X-ray images are displayed in the standard orientation with north up and east to the left. The coordinate system used throughout the paper is J2000.

For all analyses of radial distributions, projections, and spectra, point sources were detected and then excluded (231 for *Chandra*), as was the bright M87 nucleus and jet.

### 2.1. *Chandra*

M87 was observed with *Chandra* on 2000 July 29–30 (ObsID 352) and 2002 July 6–8 (ObsID 2707) for 37 and 105 ks, respectively, with ACIS-S at the focus. Details for the 2000 July and 2002 July observations are given by Young et al. (2002) and Jordan et al. (2004), respectively. The 2002 July observation was used by Jordan et al. (2004) to analyze the point-source population of M87. Sparks et al. (2004) used the *Chandra* observations to study the relationship between the X-ray structures and those seen in H $\alpha$ . They discussed the effects of thermal conduction on the hot, X-ray-emitting, and cooler, H $\alpha$  emitting, gas. As part of our analysis, we applied standard screening to the event list, excluded intervals with high background, and omitted *ASCA* grades 1, 5, and 7, known hot pixels, bad columns, and chip node boundaries.

Because the Virgo Cluster is both bright and extended, we used the ACIS-S1 chip to monitor the instrument background rate in the energy band 2.5–6.0 keV (see M. Markevitch 2001, *Chandra* calibration memo<sup>8</sup>). We found significant background flaring in both observations, and the corresponding time intervals were removed. The remaining exposure times for ObsID's 2707 and 352 were 87.9 and 30.0 ks, for a total observation time of 117.9 ks. For all imaging analyses, we generated images, exposure maps, and backgrounds separately and then combined

the results in sky coordinates. We normalized the exposure maps between frontside- and backside-illuminated CCD's, assuming the emission was characterized by thermal emission from hot gas with  $kT = 2$  keV. For spectral analyses, we extracted spectra separately from each observation and fit the spectra jointly in XSPEC. Response matrices and effective areas were averaged by weighting by the observed X-ray emission.

### 2.2. *XMM-Newton*

*XMM-Newton* observed M87 for 57.4 ks on 2000 June 19. Details of this observation are given by Bohringer et al. (2001) and Belsole et al. (2001). We report on results obtained with the MOS instrument. Calibrated event lists were generated using SAS version 5.3. The MOS background was calculated using the blank field data accumulated over a large number of observations (Lumb et al. 2002). For analysis, we used MOS data with patterns in the range 0–12 and the recommended value of the flag (XMM\_EA). For generating the temperature map, we used one of the MOS response matrices provided by the XMM-SOC and assumed that the same response (corrected for energy-dependent vignetting) is applicable for all regions. The gas temperature map was calculated as described by Churazov et al. (1996; see also Churazov et al. 2003 for this method applied to *XMM-Newton* data for the Perseus Cluster). An adaptive smoothing also was applied to the map, so that each value of the temperature was calculated using regions containing  $\sim 3600$  counts. Comparison of the overall structure with the results of direct spectral fitting of individual regions shows good agreement.

### 2.3. *ROSAT* HRI

M87 was observed seven times with the *ROSAT* HRI between 1992 and 1997 (*ROSAT* sequence numbers rh700214, rh702081, rh704000, rh701712, rh702774, rh701713, and rh702775) for a total observation length of 171.6 ks. A detailed description of the *ROSAT* HRI observations is given by Harris et al. (1999a, 1999b). We generated images from each observation using PHA channels 3–9 to reduce the instrumental background and improve the signal-to-noise ratio (S/N) for the diffuse emission. The images were then summed for further analysis.

## 3. X-RAY IMAGING

X-ray images of the two merged M87 *Chandra* observations are shown in Figures 1 and 2. Figure 1a shows the central region at full resolution (1 pixel =  $0''.492$ ) in the energy band 0.5–2.5 keV. Figure 1b covers a slightly smaller region and includes 6 cm radio contours. Figure 1c labels the features discussed in the text below. Figure 2 is an adaptively smoothed image. On the smallest scales, Figures 1 and 2 show:

1. The well-known X-ray jet extending  $\sim 20''$  from the nucleus, with the brightest emission coming from the nucleus and knot A, and showing emission from at least seven knots (Marshall et al. 2002; Harris et al. 2003).

2. X-ray cavities surrounding the jet (including one surrounding the location of the unseen counterjet), with an overall extent described as an ellipse with semimajor and semiminor axes of  $40''$  and  $15''$ , respectively, oriented along the jet direction (approximately west-northwest) and coincident with the bright radio emission seen at 6 cm (see Fig. 1b). The radio lobe cavities, particularly the counterjet cavity, are delineated by bright rims of X-ray emission.

3. An X-ray cavity (with a radius of about  $12''$ ), delineated by a bright X-ray rim, coincident with radio-emitting plasma budding from the southeast of the 6 cm radio lobes.

<sup>8</sup> See ACIS Background memo at <http://cxc.harvard.edu/contrib/maxim/bg/index.html> and a file describing how to use the tools and the background data at <http://cxc.harvard.edu/contrib/maxim/acisbg/COOKBOOK>.

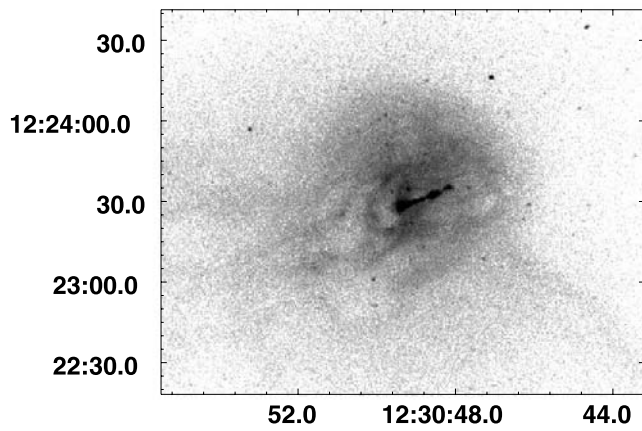


FIG. 1a

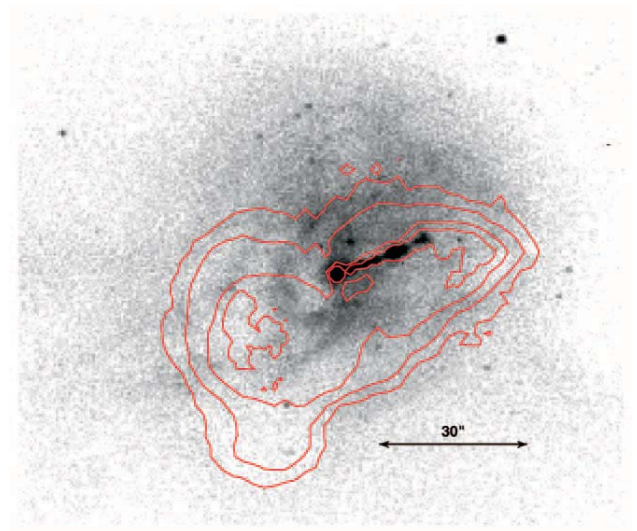


FIG. 1b

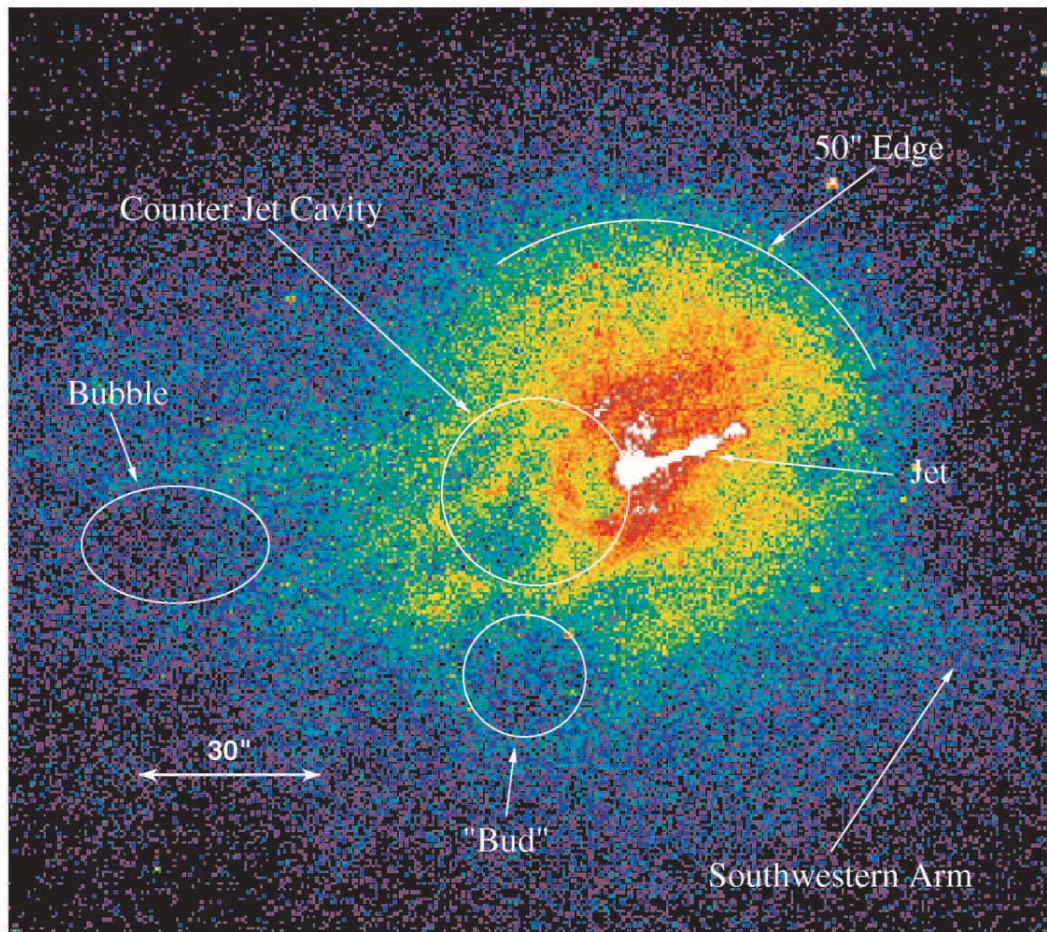


FIG. 1c

FIG. 1.—(a) Central region of M87 as seen by the *Chandra* ACIS-S detector in the energy band 0.5–2.5 keV with a Gaussian smoothing of 1 pixel =  $0''.492$ . Several cavities are seen in the counterjet direction, as is the beginning of the large-scale eastern arm. (b) Same image at a slightly larger scale, with contours (1, 5, 20, and  $45 \times 10^{-5}$  Jy per  $0''.1 \times 0''.1$  pixel) from the 6 cm radio observations of Hines et al. (1989) superposed on the X-ray image. A “bud” of radio-emitting plasma fills the X-ray cavity to the southeast. The region referred to as the cocoon in the text is the radio-emitting plasma-filled region defined by the radio contours (excluding the bud). X-ray filaments surround the bubbles in the eastern arm. (c) Identifies features discussed in the text. All images of M87 are shown with standard astronomical orientation with north up and east to the left, and the coordinates in (a) are J2000.



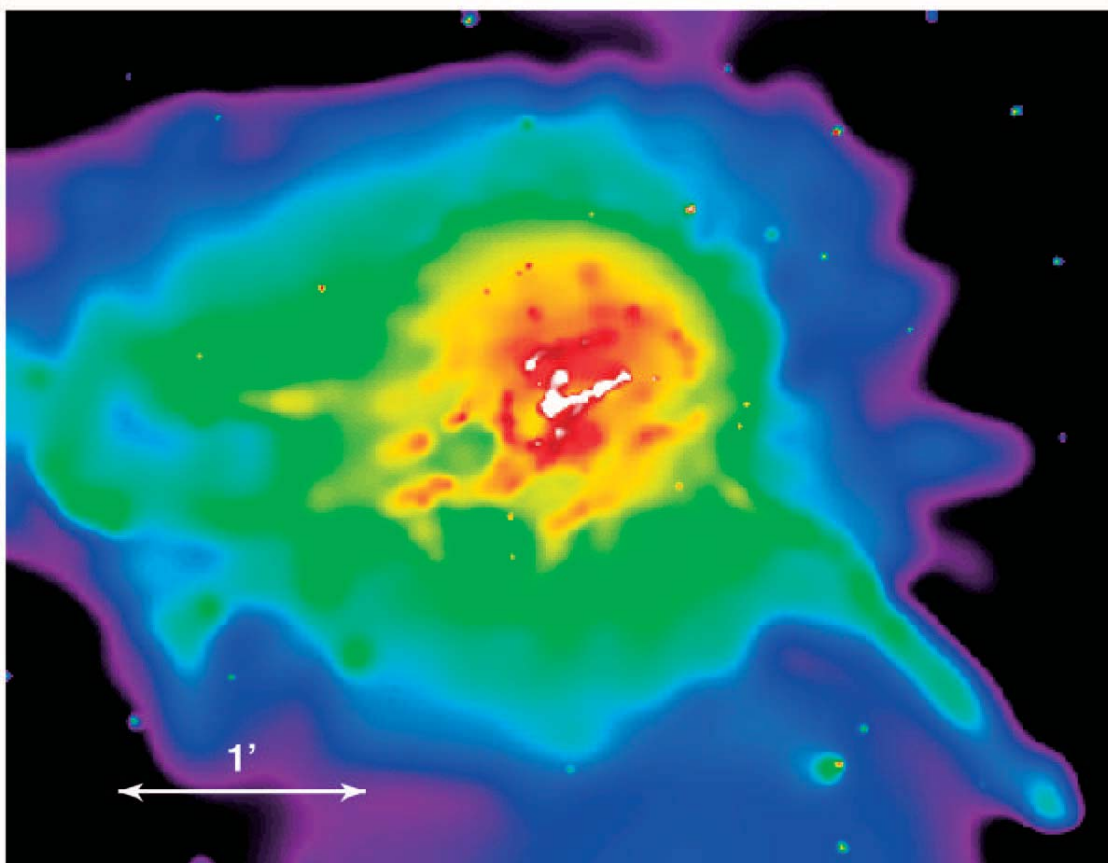


FIG. 2.—Adaptively smoothed *Chandra* image (minimum significance  $4\sigma$ ) of the central region of M87. Prominent features include the narrow southwestern arm, the bright  $50''$  radius inner core (yellow), which shows an especially sharp jump in surface brightness along the northern edge, and multiple bubbles and surrounding filaments in the core, which form the base of the eastern arm.

4. An X-ray bright core region, surrounding the 6 cm radio lobes, with a radius of approximately  $50''$ , with more pronounced emission to the north (overexposed region in Fig. 3). Young et al. (2002) suggested that an edge at the 3.9 kpc radius arises from sound waves driven by nuclear activity. Alternatively, this structure could originate either as a cold front (see the *XMM-Newton* temperature map in Fig. 6) or as a sheath of cool material surrounding the cocoon. The southern edge of the radio cocoon is bounded by a bright X-ray rim (just south of the outermost radio contour in Fig. 1b).

5. At least four cavities (typical scales of  $\sim 10''$ ) extending into the eastern arm, with associated filamentary structures that surround them.

To study the emission on larger scales, we used the *Chandra* ACIS-S2 and S3 CCDs, as well as the *ROSAT* HRI and *XMM-Newton* observations of M87. The *Chandra* large-scale image was prepared by (1) extracting the 0.5–2.5 keV images from each pointing, (2) generating “exposure” maps (accounting for vignetting, quantum efficiency, and bad pixel/columns/gaps with an assumed  $kT = 2$  keV thermal spectrum to normalize the front- and backside CCD chips), (3) smoothing (Gaussian fit of  $1''$ ) each of the images and exposure maps, (4) dividing each image by its exposure map, and (5) summing the two flat-fielded images. The resulting *Chandra* image is shown in Figure 3.

To enhance the view of the faint asymmetric structures, we processed the *Chandra*, *XMM-Newton* and *ROSAT* images to remove the large-scale radial surface brightness gradient.

Figures 4 and 5 show the relative deviations of the surface brightness from a radially averaged surface brightness model ( $\beta$  model for *Chandra* and *ROSAT*, with  $a = 8''.86$  and  $\beta = 0.37$ , and an azimuthal average for *XMM-Newton*), i.e.,  $[\text{Data} - \text{Model}]/\text{Model}$ . These images show evidence on large scales for buoyant bubbles and energetic outbursts powered by the supermassive black hole in the M87 nucleus. These features, outside the  $1'$  core, are labeled in Figures 4b and 5. The features include

1. A nearly azimuthally symmetric ring of emission with a leading edge at a radius of 14 kpc ( $3'$ ) most prominent to the north and northwest (see Figs. 3 and 4), which we interpret as a weak shock (see below).

2. A second partial ring (i.e., arc) of enhanced emission, just beyond the 14 kpc ring, at a radius of 17 kpc, most prominent at azimuths of  $0^\circ$ – $60^\circ$  from the west (see Fig. 4), which we also interpret as a shock.

3. The prominent eastern and southwestern arms that brighten significantly at approximately the radius of the 14 kpc ring.

4. The division of each arm into two filaments at radii beyond the 14 kpc ring. For the southwestern arm, the filaments (labeled S1 and S2 in Fig. 4b) turn east, while for the eastern arm, the two filaments (labeled E1 and E2 in Fig. 4b) turn north.

5. A southern arc, at a radius of approximately 37 kpc ( $\sim 8'$ ) seen in *Chandra*, *ROSAT* HRI, and *XMM-Newton* images (Figs. 4 and 5).

6. On the largest spatial scales, the *ROSAT* HRI and *XMM-Newton* images in Figure 5 show depressions in surface brightness

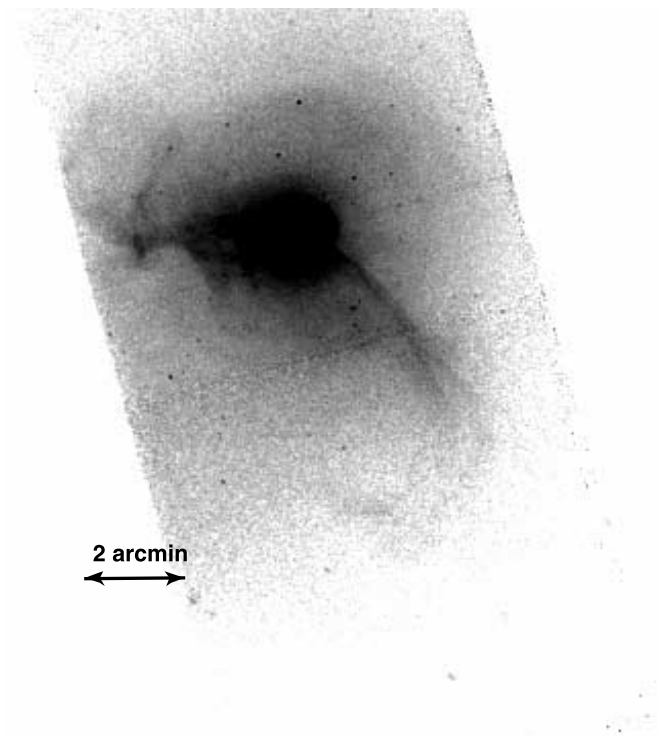


FIG. 3.—Merged, flat-fielded *Chandra* image in the energy band 0.5–2.5 keV generated by summing the two pointings after flat-fielding and smoothing each separately (see text for details). The prominent eastern and southwestern arms are apparent, as is the surface brightness enhancement with an outer edge at a  $3'$  radius from the nucleus.

to the northeast and southwest and corresponding excesses to the southeast and northwest (see regions marked “Excess” in Fig. 5a).

#### 4. XMM-NEWTON TEMPERATURE MAP

The *XMM-Newton* temperature map with its large field of view and high S/N (compared to *Chandra*) is shown in Figure 6 and is consistent with the discrete temperature fits performed by Molendi (2002; see also Belsole et al. 2001). The continuous nature of our map clearly shows some of the large-scale structures. The eastern and southwestern arms are distinctly cooler than the surrounding gas, although we found no abundance differences between the arms and the ambient M87 atmosphere. The temperature map shows, at least as clearly as the surface brightness map, the clockwise rotation to the east of the southwestern arm.

Perhaps the most striking feature of the temperature map is the similarity of the eastern and southwestern arms. In particular, the temperatures are similar, and at the end of the arms, when they start to deviate from the approximately linear structure, each bends clockwise.

#### 5. ANALYSIS AND INTERPRETATION

We discuss the origin of prominent X-ray features seen in the *Chandra*, *ROSAT* HRI, and *XMM-Newton* images in terms of energetic outbursts from the supermassive black hole at the M87 nucleus. Previous authors have provided ages for the eastern and southwestern arms and buoyant bubbles ( $10^7$  yr; Churazov et al. 2001) and the outer radio lobes ( $10^8$  yr; Owen et al. 2000). We note that while we describe the outer radio lobes as buoyant

bubbles, they must be continuously resupplied with energetic particles, as Owen et al. (2000) have emphasized.

##### 5.1. Gas Density and Temperature Deprojection

To obtain ambient gas density and pressure profiles (see Fig. 7), we deprojected the X-ray surface brightness and gas temperatures in a sector north of the nucleus at azimuths (from the north) between  $-30^\circ$  and  $45^\circ$ , a region chosen for its relative absence of asymmetric structure. The deprojection is standard (Nulsen et al. 2002), except for the handling of weights for the outermost region. Because the outer edge of the region is well within the cluster, a model was needed to allow for cluster emission beyond the deprojected volume. This was done by assuming that the surrounding gas is isothermal, with a power-law density profile ( $n_e \propto r^{-1.09}$ , which accurately matches the profile from  $1'-5'$ ; see Fig. 7c). The outermost ring was assumed to represent emission from the surrounding gas, and its weight was determined accordingly in the spectral deprojection.

##### 5.2. X-Ray Core and Inner Radio Lobes

The inner radio lobes, the cocoon region, originated in an episode of recent nuclear activity. We can use the X-ray observations to estimate the energetics associated with their formation. The counterjet cavity is well described as an ellipse with semi-major axes of  $15''$  and  $19''$  on the plane of the sky (see Fig. 1c). Using the innermost gas temperature of 1.65 keV from our deprojection (Fig. 7), and assuming the transverse expansion of the cavity is subsonic, we estimate that its age is more than  $1.7 \times 10^6$  yr. The one-sidedness and superluminal motion of the jet suggest that its path is close to our line of sight. If the axis of the cavity makes an angle of  $20^\circ$  to the line of sight (Biretta et al. 1999), then its linear dimension is about 9 kpc. Using the age estimated above, the head of the cavity is advancing at  $< 5 \times 10^3$  km s $^{-1}$ . If the cavity is  $10^7$  yr old, the average speed of the head of the cavity is significantly smaller and only mildly supersonic.

If the cavity is prolate and lies in the plane of the sky, its volume is  $\simeq 2.4 \times 10^{65}$  cm $^3$ . Using the pressure for the innermost ring of our deprojection (centered at a radius of  $22''$ ), gives  $pV = 1.3 \times 10^{56}$  ergs. If the cavity is relativistic (and the presence of the synchrotron-emitting plasma strongly argues in favor of this), then its enthalpy is  $4pV$ ; otherwise it is  $2.5pV$ . If the cavity projected as a sphere on the plane of the sky is actually a prolate ellipsoid with a  $20^\circ$  angle between the line of sight and the axis of the ellipsoid, then the volume of the cavity increases by a factor of  $\sim 2.9$ , and the center of the cavity shifts to a larger radius by the same factor. At this position, the gas pressure is 2.6 times smaller, so that our estimate of the enthalpy is only slightly altered, based on the assumption that the pressure inside the cavity is uniform (due to the high sound speed of the relativistic gas). Note that the fact that the external pressure changes over the extent of the cavity implies that the configuration must be dynamic: either parts of the lobe far from the nucleus (where the external pressure is lower) are overpressured and thus expanding into the gaseous atmosphere, or the inner parts, close to the nucleus, are underpressured, and thus collapsing, or both. The maximum overpressure of a factor of 2.6 would imply that the head of the cavity is advancing at a Mach number of 1.5. Since the cavity itself is likely oriented close to the line of sight, it is quite possible that the assumption of sphericity breaks down in the inner bins and that the derived pressure is therefore an overestimate. In either case, a detailed hydrodynamical model is needed to make a more accurate estimate

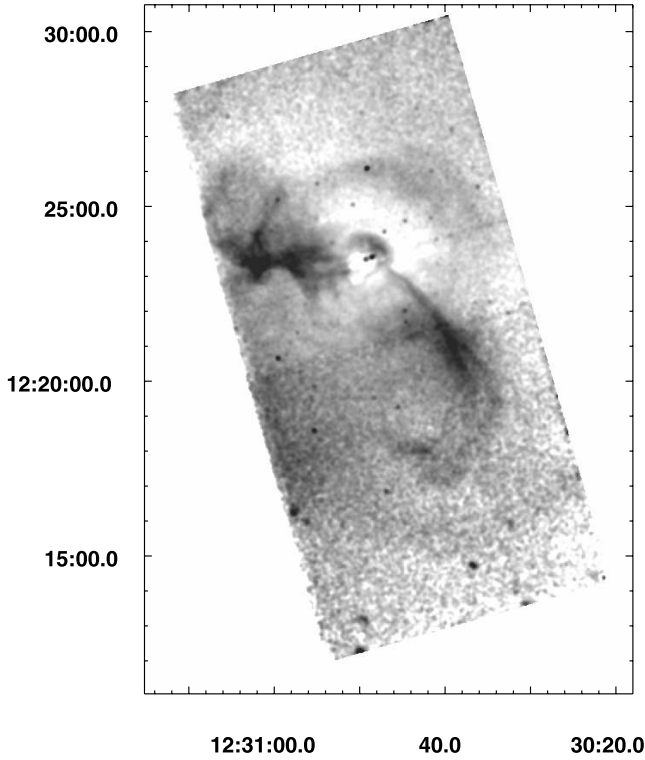


FIG. 4a

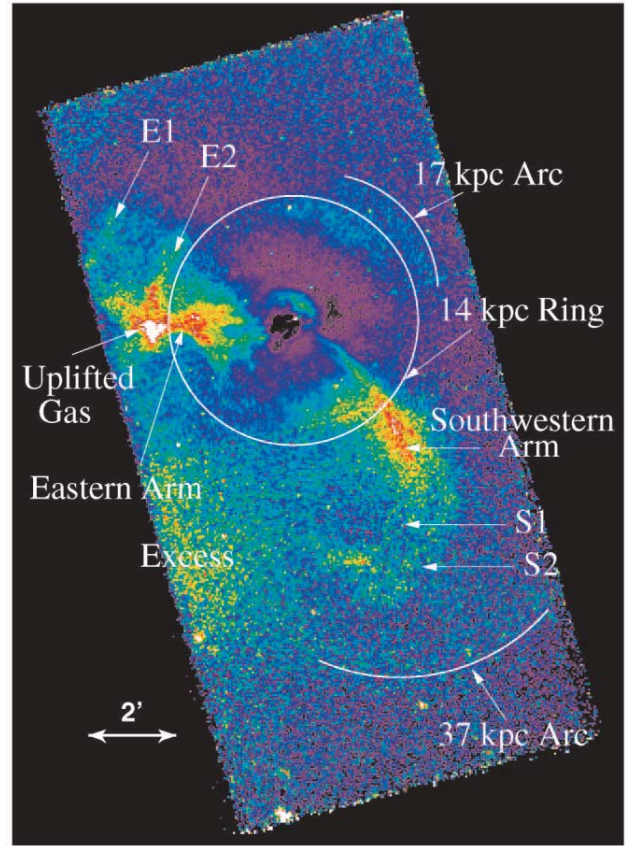


FIG. 4b

FIG. 4.—*Chandra* image (0.5–2.5 keV) processed as described in the text to remove the large-scale radial surface brightness gradient. Many faint features are seen, including, (1) the bifurcation of the eastern and southwestern arms, (2) the brightening at the eastern and southwestern arms, (3) the 14 kpc (3′) ring, (4) the 17 kpc (3′75) arc, and (5) the faint southern 37 kpc (8′) arc. The features are labeled in the color image. The 14 kpc ring and 17 kpc arc are labeled at their outer extents. Labels identify the extensions of the eastern (E1, E2) and southwestern (S1, S2) arms after each has divided. The uplifted gas core (white in the color image) that lies at the end of the eastern arm at the (projected) center of the radio torus is labeled. Note that several cavities are seen at the base of the eastern arm. In addition to the bud and the cocoon, there is a cavity at R.A. = 12<sup>h</sup>30<sup>m</sup>54<sup>s</sup>.6 decl. = +12°23′15″ (labeled in Fig. 1c) and several to its south. Coordinates are epoch J2000.

of the enthalpy, but it is unlikely to increase over our estimate by more than 50% and certainly not by more than a factor of 2.6. Doubling the calculated enthalpy to allow for the jet cavity to the west, our best estimate for the total enthalpy of these cavities is  $\simeq 1.1 \times 10^{57}$  ergs and not more than  $2.9 \times 10^{57}$  ergs, 2.6 times larger. Additional radio-emitting plasma and X-ray cavities (plasma bubbles) are observed beyond the jet cavities. Therefore, given the bubble formation time calculated below, this material is probably produced in the current outburst as well. Including this material would at most double the total enthalpy of the radio plasma from the outburst.

### 5.3. Azimuthal Rings

#### 5.3.1. The 14 kpc (3′) and 17 kpc (3′75) Rings

The 14 kpc ring is the clearest example of a shock-driven feature in M87. Although most prominent to the north and west, it is seen over nearly 360° in the azimuth centered on the M87 nucleus (Fig. 4). As described in § 5.1, we measured the surface brightness and temperature profiles in a sector north of the nucleus. The deprojected gas density profile is shown in Figure 7, along with the deprojected gas temperature. If we identify the inner radio lobes with the piston that drives this shock, since they are small compared to the volume encompassed by the ex-

panding front, the event that drove the shock may be treated as instantaneous. If the shock is expanding into a spherically symmetric medium, it will become increasingly spherical, regardless of the shape of the initial outburst. Thus we model the outburst required to generate the 14 kpc ring by assuming that energy is injected in a single event into the atmosphere by the central AGN. Our estimate of the outburst energy is robust to varying details of the actual outburst. Before the passage of the shock, the gaseous atmosphere is hydrostatic and isothermal, with a power law density profile  $n_e \propto r^{-1.09}$ , chosen to match the surface brightness profile immediately outside the shock. We derived the parameters of the outburst by matching calculated surface brightness profiles to that observed and verifying that the temperature data were consistent with those calculated. The model that best matches the data is characterized by an energy deposit of  $8 \times 10^{57}$  ergs about  $10^7$  yr ago and is shown in Figure 7c, compared to the observed surface brightness distribution. The shock is mildly supersonic, with  $M = v/c_s = 1.2$  ( $v = 950$  km s<sup>-1</sup>). A weak temperature enhancement at the position of the ring (Fig. 7) is consistent with the calculated model (as is the slight temperature reduction inward of the shock). Although the temperature evidence is not strong, the remarkably spherical appearance of this feature is compelling evidence that it is a weak shock driven by the AGN. This description for



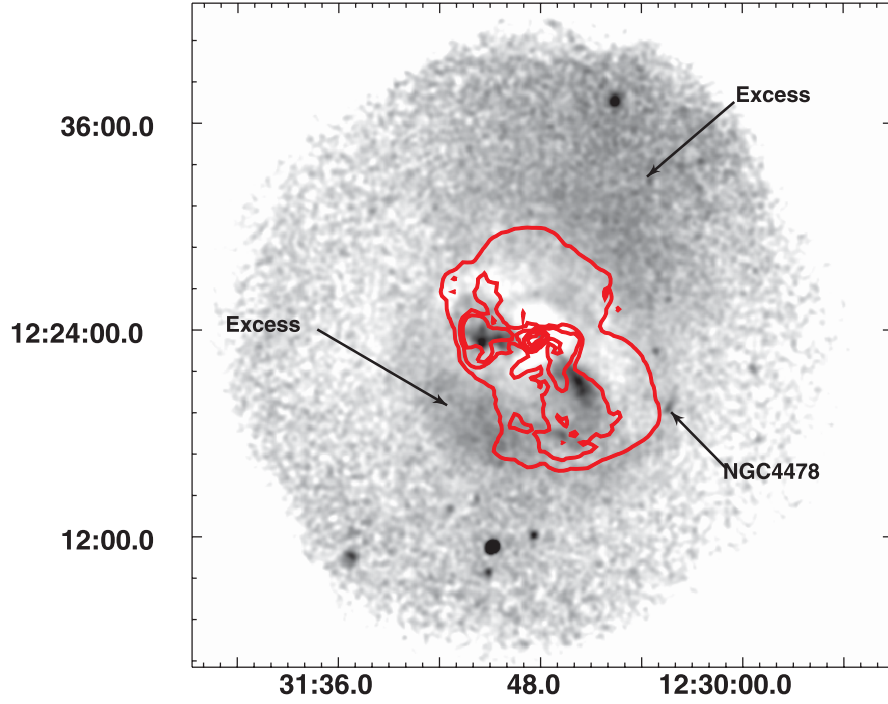


FIG. 5a

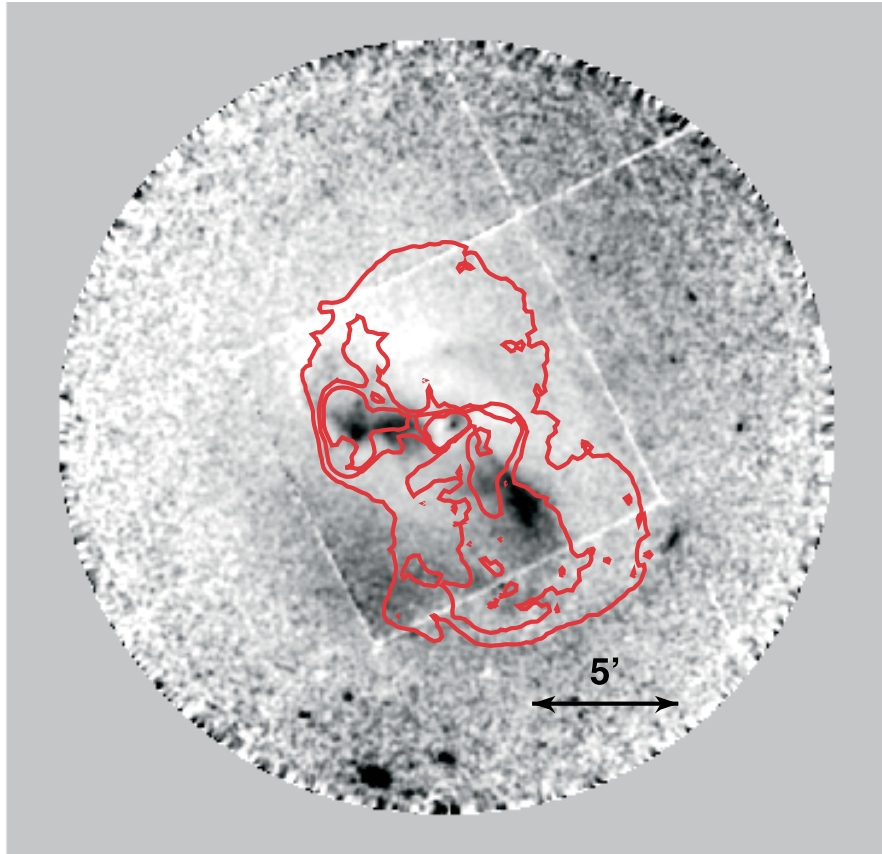


FIG. 5b

FIG. 5.—(a) *ROSAT* HRI and (b) *XMM-Newton* MOS1 + MOS2 images processed to remove the steep radial surface brightness gradient. Both figures show asymmetric emission on large scales (beyond the outer radio lobes). The diffuse emission (labeled “Excess” in the *ROSAT* HRI image) is bright both to the east of the southern radio lobe and to the north of the northern lobe. Asymmetric gas distributions at radii of  $\sim 50$  kpc may be evidence for older ( $>10^8$  yr) outbursts, as are the outer radio lobes. The extended emission from NGC 4478 (labeled in the *ROSAT* HRI image) and the southern 37 kpc arc (just outside the outer contour of the southern radio lobe) are seen in both the *ROSAT* HRI and *XMM-Newton* images. Contours at  $2 \times 10^{-4}$ ,  $2 \times 10^{-3}$ ,  $4 \times 10^{-3}$ ,  $4 \times 10^{-2}$ , and  $2 \times 10^{-1}$  Jy per  $1''.5 \times 1''.5$  pixel from the 90 cm radio map (Owen et al. 2000) are shown. Coordinates are epoch J2000.

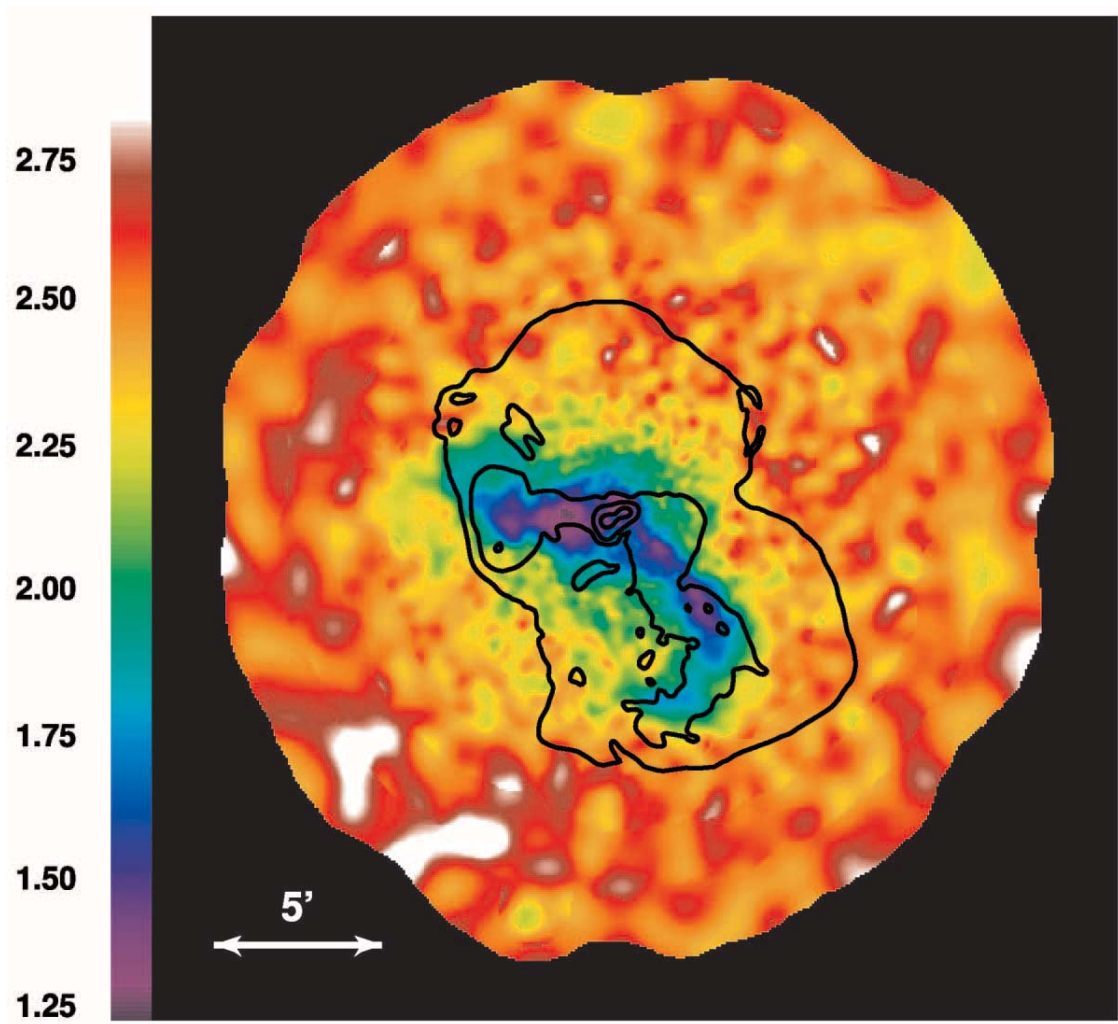


FIG. 6.—*XMM-Newton* temperature map generated according to the method described by Churazov et al. (1996) and summarized in the text. The eastern and southwestern arms are cooler than the ambient gas (as already discussed in earlier *XMM-Newton* analyses, e.g., Belsole et al. 2001 and Molendi 2002). The temperature map is adaptively smoothed to reduce the noise, and hence small scale features are necessarily broadened. Contours from the 90 cm image from Owen et al. are superposed ( $0.25, 2.5, 25$ , and  $250 \times 10^{-3}$  Jy per  $1''.5 \times 1''.5$  pixel).

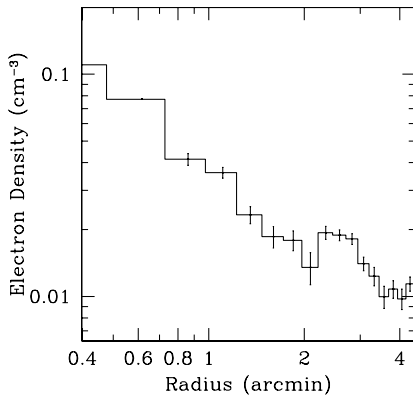


FIG. 7a

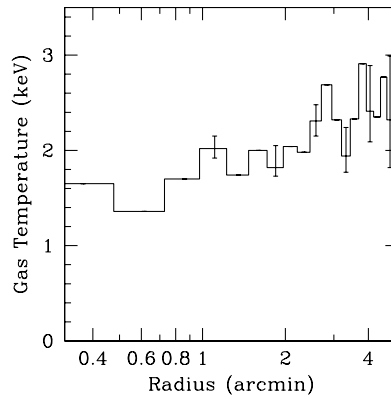


FIG. 7b

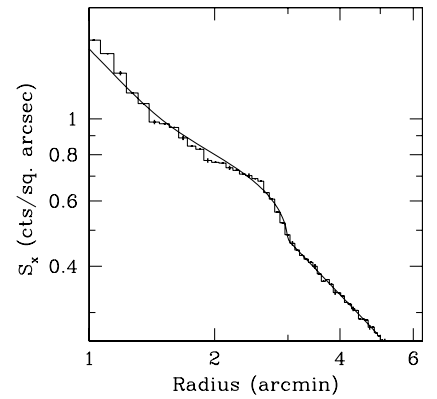


FIG. 7c

FIG. 7.—(a) Radial electron density profile shows the 14 kpc ( $3'$ ) ring. (b) Deprojected gas temperature. (c) Model compared to the observed surface brightness profile. The deprojected gas density and temperature are derived by fitting the outermost bin and then using the fit results, weighted by the projected emissivity of the outermost ring, as one component of the fit for the next inner ring. Repeating this process inward yields the deprojected temperature and density profile. We use the deprojected values of gas density and temperature to calculate gas pressures.

the formation of the 14 kpc ring is similar to that of Ruszkowski et al. (2004), in which impulsive energy injection generates weak shocks as the injected energy forms a cocoon in the galaxy atmosphere in the Virgo core. We note that the time estimate,  $1.1 \times 10^7$  yr, for the onset of the activity that gave rise to the 14 kpc ring is robust, and the simple model gives this age to an accuracy of about 10%.

A second partial ring is seen to the west at a radius of 17 kpc ( $3.75^\circ$ ) extending over  $\sim 60^\circ$  in the azimuth (see Fig. 4c). To form this surface brightness enhancement, a disturbance traveling at the sound speed would have originated approximately  $4 \times 10^6$  yr before the event that created the 14 kpc ring. The amplitude of the 17 kpc ring is comparable to that of the 14 kpc ring and therefore would require a similar amount of injected energy. The timescale between the two events lies well within the range,  $10^5$ – $10^8$  yr, expected for repetitive AGN outbursts.

In our shock model for the 14 and 17 kpc rings, one or both may be associated with the inflation of the inner cocoon. This is consistent with radio source models in which the radio outburst commences with rapid expansion, driving a shock. As the expansion slows, the shock separates from the driver, weakens, and becomes more spherical (the “sonic boom phase” in Reynolds et al. 2001). The current energy input by the jet is estimated to be  $10^{44}$  ergs  $s^{-1}$  by Bicknell & Begelman (1996). Owen et al. (2000) used the radio observations to derive a minimum value of the instantaneous energy input by the jet of a few  $\times 10^{44}$  ergs  $s^{-1}$ . The energy input is more than sufficient to power the lobes and generate a roughly spherical pulse.

The spherical shock model provides an estimate of the total energy in the outburst. This energy is significantly greater (a factor of 3 or more) than the enthalpy of the cavities also created by the AGN outburst (see § 5.2). This suggests that shocks may be the most significant channel of AGN energy input into cooling-flow atmospheres in early-type galaxies, groups, and galaxy clusters. Fabian et al. (2003) find similar shocks and “edges” around NGC 1275 in the Perseus Cluster. They also argue that the energy deposited as these features dissipate can compensate for the energy radiated by the cooling gas in the inner 50 kpc core. For M87, the mean power of the shock outburst averaged over the past  $10^7$  yr is  $2.4 \times 10^{43}$  ergs  $s^{-1}$ . Within 70 kpc, the radiative loss from the cooling flow is  $\sim 10^{43}$  ergs  $s^{-1}$  (corresponding to  $10 M_\odot$   $yr^{-1}$ ; Stewart et al. 1984). Thus, one such outburst every  $3 \times 10^7$  yr is sufficient to quench the cooling flow in the absence of any other heat source. In addition to the energy input from the outburst we have modeled, energy is also being supplied by the buoyantly rising features seen in the radio maps (Churazov et al. 2002).

### 5.3.2. Southern 37 kpc ( $8'$ ) Arc

South of the nucleus at a radius of 37 kpc ( $8'$ ), a surface brightness enhancement appears as an arc or partial ring in observations by *Chandra*, *ROSAT* HRI, and *XMM-Newton* (see Figs. 4 and 5). This partial ring extends over an azimuth of at least  $45^\circ$ . Statistically, its significance is shown in the radial profile in Figure 8 made from the *Chandra* image. As Figure 5 shows, the southern 37 kpc arc lies just outside the large-scale radio lobes characterized by Owen et al. (2000) as the oldest ( $10^8$  yr) structures in M87. In the model by Churazov et al. (2001), these radio lobes were originally buoyant bubbles that have risen in the gaseous atmosphere surrounding M87 and are now thin disks (“pancakes”) seen in projection. Each  $10^8$  yr old bubble is partially surrounded by gas that has been displaced by the bubble’s rise. This gas could be material piled up

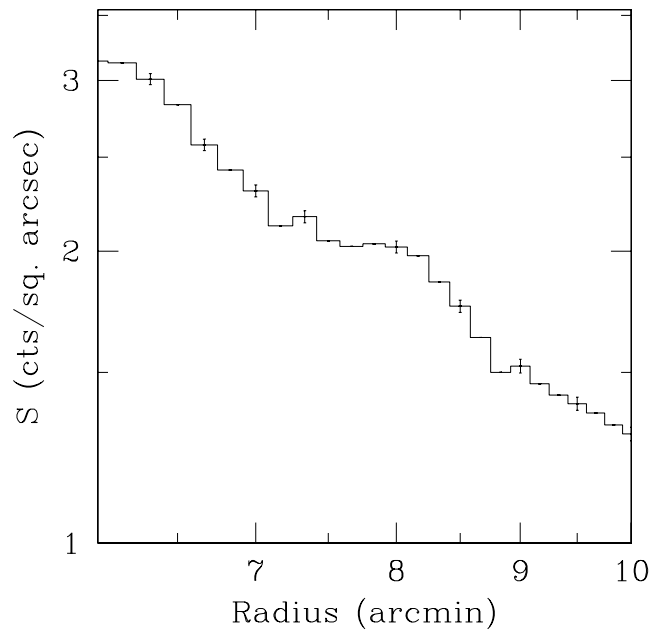


FIG. 8.—Radial profile extracted from the merged *Chandra* image (0.5–2.5 keV) showing the excess emission 37 kpc from the nucleus of M87. The profile was extracted over an azimuth of  $30^\circ$ .

on the edge of the bubble during its expansion or alternatively, gas that was uplifted by the bubble and is draining off the bubble along its sides. The *XMM-Newton* spectra show that the gas associated with this feature has a similar temperature ( $kT \approx 2.5$  keV) but high abundance ( $1.2 \pm 0.3$  of solar for an APEC model) compared to other gas at the same radius (0.4–0.5 of solar).

Rims of cool gas are a common feature of cavities created by radio lobes (e.g., Finoguenov & Jones 2001; McNamara et al. 2000; Fabian et al. 2002; Blanton et al. 2001). In M87 we see rims most clearly in the bright edge of the counterjet cavity, the southeastern “bud,” and the southern edge of the outer radio lobes. The presence of bright rims over such a wide range of scales illustrates the ability of the radio plasma to exclude hot gas and attests to their surprising stability (Nulsen et al. 2002).

At the western end of the 37 kpc arc, a brightness enhancement is seen in both the *XMM-Newton* and *ROSAT* HRI images (Fig. 5). This feature is extended from northwest to southeast ( $30''$ , 2.3 kpc, in length) and is likely associated with a Virgo Cluster member, the E2 galaxy NGC 4478 (R.A. =  $12^h30^m17.4^s$ , decl. =  $+12^\circ19'43''$ ), which is coincident with the X-ray feature. The X-ray luminosity of the galaxy is  $7 \times 10^{38}$  ergs  $s^{-1}$ , and its optical absolute magnitude is  $M_B = -18.8$  (for a distance of 16 Mpc). The X-ray and optical luminosities are consistent with the  $L_X - M_B$  correlation for the emission from hot gas in early-type galaxies (e.g., Forman et al. 1985). David et al. (1991) showed that early-type galaxies with  $M_B = -19$  would be transitioning from atmospheres with partial to total subsonic winds, assuming a supernova rate of 0.15 SN Ia per  $10^{10} L_\odot$  per century (van den Bergh et al. 1987). If the supernova rate in NGC 4478 is slightly less than this assumed value or if some fraction of the supernova energy is not transferred to the hot atmosphere, then NGC 4478 could maintain a barely stable atmosphere. Such an atmosphere could be ram pressure stripped in the dense Virgo core, producing the extended X-ray emission seen in the *ROSAT* HRI and *XMM-Newton* images. Thus, most likely we are observing the gaseous halo of an elliptical galaxy being

stripped by the atmosphere around M87, and the feature is probably not associated directly with the southern arc.

### 5.3.3. Large-Scale Surface Brightness Asymmetries

On the largest scales, the *XMM-Newton* and *ROSAT* images (Fig. 5) show surface brightness enhancements and depressions outside the outer radio lobes and beyond the 37 kpc arc. As a particular example of the magnitude of these variations, in  $30^\circ$  wide sectors at a radius of  $50 \pm 5$  kpc ( $11'$ ), the surface brightness in the *ROSAT* HRI has a maximum 18% above the mean in the northwest and a minimum 10% below the mean in the southwest. At somewhat smaller radii, Figure 5 shows higher surface brightness to the southeast, just beyond the outer radio lobe.

Some of these asymmetries could arise from an elliptical gravitational potential, or they could result from subtracting an azimuthally symmetric model for the surface brightness from an elliptical distribution. Alternatively, such an asymmetrical distribution could arise from “ghost cavities” (e.g., Ensslin 1999) of relativistic plasma, produced by earlier epochs of AGN activity but no longer emitting at observable radio frequencies. The outer radio lobes are approximately  $10^8$  yr old, and as Owen et al. (2000) argued, their detection requires ongoing energy injection. Any older cavities, at larger radii, may no longer have a connection to the nucleus and, hence, would no longer be detectable at radio wavelengths.

### 5.4. A Budding Bubble

In most systems, X-ray cavities or radio plasma bubbles generally are consistent with having been directly filled by an active jet and are aligned with the jet axis or lie on opposite sides of the active nucleus. Clear examples of such alignments include a wide variety of systems ranging from galaxies with very modest gaseous atmospheres, such as Cen A (Kraft et al. 2003) and M84 (Finoguenov & Jones 2001), to those with rich luminous clusters, including Hydra A (McNamara et al. 2000; David et al. 2001; Nulsen et al. 2002) and Perseus (Böhringer et al. 1993; Fabian et al. 2002).

While many of the inner X-ray structures in M87 are clearly aligned along the direction of the M87 jet axis, the southeastern bubble (extending from  $30''$  to  $45''$  from the M87 nucleus) is an exception (see Fig. 1). This bubble corresponds precisely to a radio feature and appears as a “bud” emanating from the southeast of the bright radio core. Figure 1b shows the X-ray image with the 6 cm radio contours superposed (Hines et al. 1989). The surrounding X-ray emission traces the outline of the outer radio contour and shows that the X-ray cavity is filled with radio-emitting plasma.

The bud emanates from the inner radio cocoon (just south of the cavity corresponding to the counterjet), almost perpendicular to the axis defined by the jet. While its origin is likely associated with an outburst from the active nucleus and an episode of energy injection into the inner cocoon, the location of the bubble may mark a magnetically weak region of the inner cocoon (the counterjet cavity) with buoyancy forces driving the bubble perpendicular to the dominant axis of recent activity.

If we assume that the rise of the budding bubble (radius  $r = 11''$ , 0.85 kpc) is governed by buoyancy and limited by the drag of M87’s hot gaseous atmosphere, we can estimate the formation time,  $\tau_{\text{bubble}}$ , as the time for the bubble to rise through its own diameter, since the bubble “originates” at the edge of the cocoon. If  $R$  is the distance from the cluster center to the

current position of the bubble and  $M(R)$  is the total gravitating mass within  $R$ , then

$$\tau_{\text{bubble}} \simeq 2R \sqrt{\frac{C_W r}{GM(R)}} \simeq 4 \times 10^6 \text{ yr}, \quad (1)$$

where we have used  $R = 34''$  (2.6 kpc), the projected distance from the cluster center, and  $M(R) = 1.4 \times 10^{11} M_\odot$  (Coté et al. 2001). The drag coefficient for a roughly spherical bubble is  $C_W \sim 0.5$ . If the bubble lies out of the plane of the sky, then both  $R$  and  $M(R)$  are larger, and hence the actual rise time is larger than  $4 \times 10^6$  yr. Furthermore, with a rise time of  $4 \times 10^6$  yr through a distance of  $2r = 2 \times 0.85$  kpc, the calculated speed of the bubble,  $\sim 400 \text{ km s}^{-1}$ , exceeds half of the sound speed. Since buoyant velocities cannot be a large fraction of the sound speed, the velocity derived from 1 is likely to be an overestimate, and hence the rise time is an underestimate, even if the budding bubble lies in the plane of the sky.

During its rapid initial expansion, the boundary of the bubble will generally be stable. As a result, the motion of the bubble boundary generally needs to be subsonic before a bubble even starts to form. This adds a further delay to  $\tau_{\text{bubble}}$  after the outburst but before the bubble is formed. If we do associate the budding bubble with an energetic nuclear event, then the constraints on its formation timescale make it quite reasonable to associate it with the current outburst (associated with the jet) that commenced about  $10^7$  years ago.

### 5.5. Buoyant Bubbles and the Structure of the Eastern and Southwestern Arms

The most striking X-ray features in M87 are the two arms that extend east and southwest from the inner lobe region. These also are seen in the 90 cm image (see Fig. 11 for a composite X-ray–radio view of M87). Previous spectroscopic studies of the arms have used the *XMM-Newton* observations (Belsole et al. 2001; Molendi 2002). They find that the arms are cool and portions are poorly fit by single-temperature components. Our *Chandra* results agree with these previous analyses, as does our *XMM-Newton* temperature map (Fig. 6). We find that the arms require at least two components (with variable abundances, VMEKAL or VAPEC) with the low- and high-temperature components in the ranges 1–1.5 and 2–2.7 keV, respectively. Although the two arms are likely related to the same outburst, we discuss each separately.

#### 5.5.1. Eastern Arm

The eastern X-ray and radio arm begins at the eastern edge of the inner radio cocoon, but its appearance is much more amorphous than that of the southwestern arm (see Figs. 1, 3, and 4). At the base of the filament (Figs. 1 and 2) are at least four bubbles with sizes comparable to that of the “bud” discussed above and streamers of gas bounding these buoyantly rising bubbles. Typical bubble sizes are  $\sim 10''$  (0.8 kpc) in radius and are reminiscent of the “effervescent” heating described by Begelman (2004). Figure 9 shows a projection across one of these effervescent bubbles  $1'25$  (5.8 kpc) east of the M87 nucleus (labeled “Bubble” in Fig. 1c).

The temperature structure (Fig. 6) of the eastern arm shows X-ray features that are consistent with cool material uplifted by a rising torus, as originally suggested by Churazov et al. (2001). First, the largest concentration of the coolest gas lies midway along the eastern arm ( $1' - 2'$  from M87’s nucleus). Second, the cool gas column in the eastern arm narrows at the edge



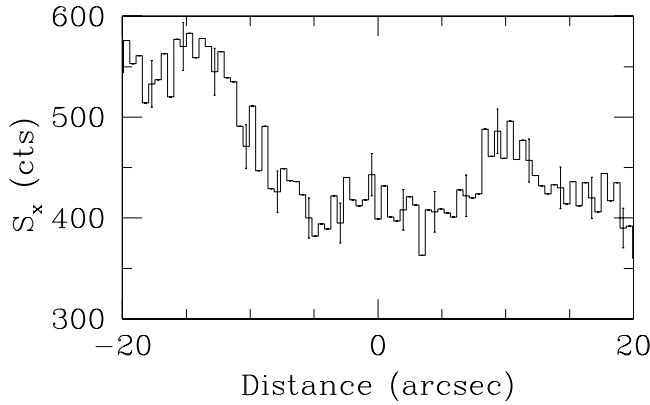


FIG. 9.—Projection across one of the effervescent bubbles at the base of the eastern arm from the merged *Chandra* data. This particular bubble is centered  $1.25$  ( $5.8$  kpc) east of the M87 nucleus (and is labeled “Bubble” in Fig. 1c). The width of the projection is the bubble diameter,  $20''$  ( $1.6$  kpc).

of the radio torus closest to the M87 nucleus and then broadens within the torus (labeled “Uplifted Gas” in Fig. 4b), just as one might expect for gas uplifted by a buoyant toroidal plasma bubble (see Fig. 11 and Figs. 3 and 4 in Churazov et al. 2001). In a detailed *XMM-Newton* analysis, Molendi (2002) performed two-temperature fits to the *XMM-Newton* spectra and found that the temperature of the cool phase does not change much as the radius increases. It was also pointed out that the entropy of the cool phase is lower than the entropy of the hot phase. These results might hint toward a more complicated picture than described by the simple simulations in Churazov et al. (2001), in which the cool phase is associated with adiabatic expansion of the hot gas entrained by the rising bubbles. For instance, relatively cool and low entropy gas may already be present close to the nucleus, while the interplay between cooling, mixing, and dissipation of kinetic energy, during the bubble’s rise, might lead to departures from adiabaticity. More detailed models are clearly needed to test the detailed properties derived from *XMM-Newton* and *Chandra* observations.

A projection along the arm, Figure 10, shows a 25% brightening at the radial distance of the 14 kpc ring. A similar brightening occurs at about the same angular distance on the southwestern arm. While the feature in the southwestern arm is partially obscured by the change from the ACIS-S3 to S2 chip in the *Chandra* image, it is clearly seen in both the *ROSAT* HRI and *XMM-Newton* images (Fig. 5). If this brightening is associated with the passage of the same shock that produced the ring, then this arm (and the southwestern arm as well) must lie close to the plane of the sky.

If this brightening does arise from the passage of the shock, it is likely that the so-called radio ear, the vortex-like structure that forms the end of the bright eastern radio filament (see Fig. 11), falls between the shocks associated with the 14 and 17 kpc rings. This could explain the flat, ringlike appearance of this radio feature, since passage of a shock through a bubble of relativistic plasma embedded in a background of cold thermal material will induce strong vorticity in the plasma, turning it into a ringlike structure (Ensslin & Bruggen 2002). Combined with the effect of vorticity creation in buoyantly rising bubbles described by Churazov et al. (2001), this could account for the filamentary appearance of this feature.

At the end of the eastern arm ( $\sim 3'$  east of the M87 nucleus), the X-ray image (Fig. 4) shows an almost circular enhancement (radius of  $1'$  centered at R.A. =  $12^{\text{h}}31^{\text{m}}05^{\text{s}}.397$ , decl. =

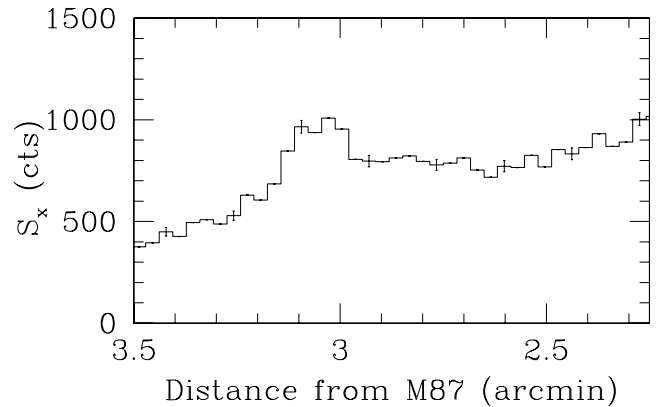


FIG. 10.—Projection along the eastern arm shows the sharp surface brightness enhancement at a radius of  $\sim 3'$ , comparable to that of the 14 kpc ring. A similar brightening is seen at approximately the same distance from the M87 nucleus along the southwestern arm (see Fig. 4).

+ $12^{\circ}25'10''.01$ ) extending to the north (beyond the northern “ear” of the radio-emitting torus). This circular feature is bounded on three sides by X-ray enhancements (see Fig. 4) that originate at the eastern arm, and it is bounded to the northwest by a pair of radio arcs (best seen in the 90 cm image; see Fig. 11). The X-ray temperature of this circular region is intermediate in temperature ( $1.8$ – $1.9$  keV), as seen in Figure 6, and is comparable to that of the end of the southeastern arm (as it swings to the east). The two enhancements, labeled E1 and E2 in Fig. 4b, which bound the circular region, appear similar to the two filaments into which the southwestern arm divides (see below). We suggest that the outer portions of the eastern arm are similar to the southwestern arm, but seen from a different orientation.

There is an unusual ionized gas cloud (R.A. =  $12^{\text{h}}31^{\text{m}}02^{\text{s}}.14$ , decl. =  $12^{\circ}24'11''.0$ ), found by Gavazzi et al. (2000), at large radii,  $3.16$ , from the center of M87, which lies in the enhancement E1 (see Fig. 4). Gavazzi et al. argue that the line diagnostics from their spectra are best described by an intermediate-velocity shock. The shock interpretation for the excitation of this cloud is consistent with its radial distance between the 14 and 17 kpc X-ray arcs, which we interpret as shocks.

#### 5.5.2. Southwestern Arm

The southwestern X-ray arm originates (see Figs. 1 and 2) as a narrow filament of width approximately  $10''$  ( $0.8$  kpc) at its narrowest, when it exits from the bright inner core (at a distance of  $50''$ ,  $3.9$  kpc from the nucleus). The filament extends in an almost straight line to the southwest for  $\sim 2'$  ( $9.3$  kpc). As seen in Figure 11, over this distance it appears uncorrelated with the radio filament that extends in approximately the same direction. At a distance of about  $3.4$  ( $15.8$  kpc), the X-ray filament bifurcates (the two sections are labeled S1 and S2 in Fig. 4c), and the correspondence between the radio plasma and X-ray gas becomes more direct. The brightest radio emission lies between the two X-ray arms as they both rotate clockwise in the plane of the sky and eventually turn due east.

Young et al. (2002) suggested that the arms are overpressurized. Assuming the southwestern arm is a cylinder lying in the plane of the sky, we find that the pressure in the arm is roughly twice that of the hotter ambient gas. We found no elemental abundance differences that could explain the surface brightness enhancement in the arms. However, the pressure difference seems unphysical, since the time for the pressure to come to equilibrium (the sound crossing time of the arm) is

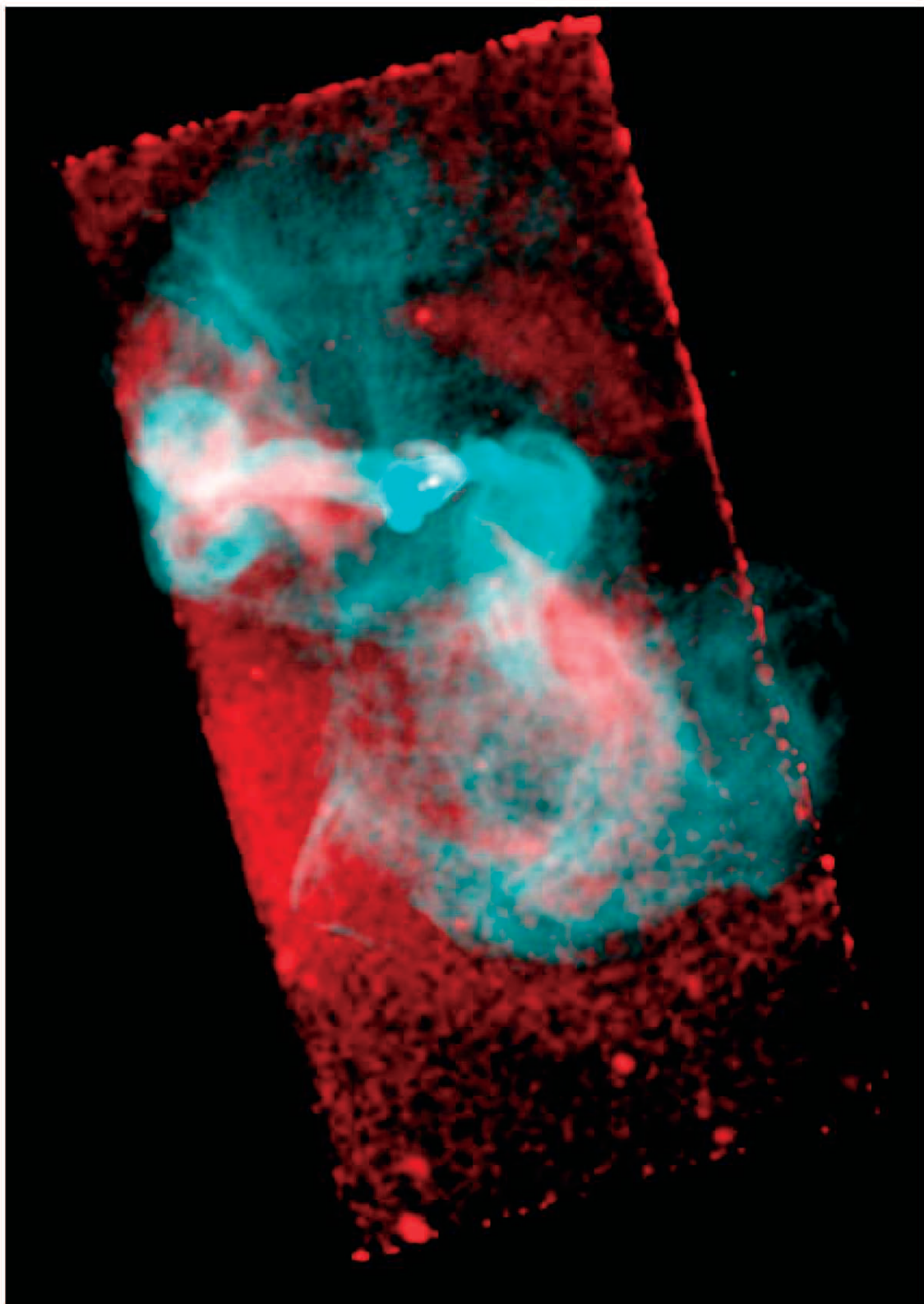


FIG. 11.—X-ray image (*red*) from Fig. 4 combined with the 90 cm radio map (*light blue*) of Owen et al. (2000) and emphasizing both the similarities and differences between the X-ray and radio emission. In the eastern arm, the X-ray and radio appear nearly coincident, as one might expect for a cool, dense X-ray column generated by buoyant bubbles. The end of the radio arm shows the clear toroidal shape expected from a large buoyant bubble. To the southwest, the radio emission appears to spiral around the narrow X-ray filament until the X-ray filament divides and bends to the east. The scale of the figure is given by the dimensions of the detector of  $8' \times 16'$ .

short compared to the sound travel time along the length of the narrow arm. Therefore, the axis of the arm would need to make a sufficiently small angle with our line of sight (roughly  $15^\circ$ ) to make its projected path length about 4 times its width, in order to account for its high emission measure. This seems unlikely, given that the brightening along the arm is at a comparable radius to that of the eastern arm and both are at a radius similar to that of the 14 kpc ( $3'$ ) ring. However, in computing the overpressure of the arm, we did not include any contribution to the external pressure from nonthermal particles or from a magnetic field, which could contribute to the confinement. Magnetic tension could also serve to confine the gas in the southwestern arm, since the radio emission from the southwestern arm appears to spiral around the X-ray gas (see Fig. 11). Alternatively, the southwestern arm may not be formed by rising bubbles, as seen in the eastern arm, but could be a thin sheath of gas exterior to a large plasma bubble related to the southwestern radio arm. This is consistent with a roughly 20% increase in surface brightness from west to east across the arm.

## 6. CONCLUSIONS

We have presented a discussion of several of the remarkable structures seen in the *Chandra*, *XMM-Newton*, and *ROSATHRI* observations of M87. Many of these, particularly the bubbles emanating from the central region, the nearly circular rings of enhanced emission at 14 and 17 kpc, and the brightening of the X-ray arms at these radii, can be attributed to AGN outbursts. The 14 and 17 kpc rings, similar to the “ripples” seen in the Perseus Cluster (Fabian et al. 2003), can be interpreted as shock

waves driven by the current outburst that began about  $10^7$  yr ago. The outburst also inflated the inner radio lobes (and cocoon). Outbursts such as those that produced these shocks can quench the M87 cooling flow, if they occur approximately every  $3 \times 10^7$  yr. Since the enthalpy associated with the inner cavities, produced by the outburst, is only 30% of the energy of the outburst, shock heating is probably the dominant heating mechanism for the gas in the inner regions of cooling-flow systems.

At larger radii, we see highly enriched gas along the outer edge of the southern radio lobe (the 37 kpc arc). Asymmetric gas distributions at radii of  $\sim 50$  kpc may be evidence for older ( $>10^8$  yr) outbursts, as are the outer radio lobes.

The hot X-ray-emitting gas contains reflections of previous episodes of AGN activity in the form of bubbles and their bright rims, shocks, and buoyantly uplifted gas structures. With the detailed observations at X-ray and radio wavelengths of M87, we can probe the interaction between the central AGN, the relativistic plasma, and the X-ray gas. We are beginning to understand the cyclic heating of the X-ray gas and the energy transfer mechanisms between the central supermassive black hole and the hot gaseous atmosphere that surrounds central cluster galaxies.

We acknowledge stimulating discussions with D. Harris, L. David, M. Begelman, and R. Sunyaev. We thank the referee, Y. Fujita, for helpful and constructive suggestions. This work was supported by NASA contracts NAS8-38248, NAS8-01130, and NAS8-03060, the *Chandra* Science Center, the Smithsonian Institution, and Max-Planck-Institut für Astrophysik.

## REFERENCES

- Bahcall, J., & Sarazin, C. 1977, *ApJ*, 213, L99  
 Begelman, M. 2004, in *Carnegie Observatories Astrophysics Series*, Vol. 1, ed. L. C. Ho (Cambridge: Cambridge Univ. Press), 375  
 Belsole, E., et al. 2001, *A&A*, 365, L188  
 Bicknell, G., & Begelman, M. 1996, *ApJ*, 467, 597  
 Binney, J. 1999, in *The Radio Galaxy Messier 87*, ed. H.-J. Roser & K. Meisenheimer (New York: Springer), 116  
 Binney, J., & Tabor, G. 1995, *MNRAS*, 276, 663  
 Biretta, J., Sparks, W., & Macchetto, F. 1999, *ApJ*, 520, 621  
 Blanton, E. L., Sarazin, C. L., McNamara, B. R., & Wise, M. 2001, *ApJ*, 558, L15  
 Böhringer, H., Voges, W., Fabian, A., Edge, H., & Neumann, D. 1993, *MNRAS*, 264, L25  
 Böhringer, H., et al. 2001, *A&A*, 365, L181  
 Bruggen, M. 2003, *ApJ*, 592, 839  
 Churazov, E., Bruggen, M., Kaiser, C., Böhringer, H., & Forman, W. 2001, *ApJ*, 554, 261  
 Churazov, E., Forman, W., Jones, C., & Böhringer, H. 2003, *ApJ*, 590, 225  
 Churazov, E., Gilfanov, M., Forman, W., & Jones, C. 1996, *ApJ*, 471, 673  
 Churazov, E., Sunyaev, R., Forman, W., & Böhringer, H. 2002, *MNRAS*, 332, 729  
 Coté, P., et al. 2001, *ApJ*, 559, 828  
 David, L., Forman, W., & Jones, C. 1991, *ApJ*, 369, 121  
 David, L., et al. 2001, *ApJ*, 557, 546  
 De Young, D. 2003, *MNRAS*, 343, 719  
 Ensslin, T. 1999, in *Proceedings of the Workshop Diffuse Thermal and Relativistic Plasma in Galaxy Clusters*, ed. H. Böhringer et al. (Garching: MPI extraterr. Phys.), 275  
 Ensslin, T., & Bruggen, M. 2002, *MNRAS*, 331, 1011  
 Fabian, A. 1994, *ARA&A*, 32, 277  
 Fabian, A., Celotti, A., Blundell, K., Kassim, N., & Perley, R. 2002, *MNRAS*, 331, 369  
 Fabian, A. C., Sanders, J. S., Allen, S. W., Crawford, C. S., Iwasawa, K., Johnstone, R. M., Schmidt, R. W., & Taylor, G. B. 2003, *MNRAS*, 344, L43  
 Fabricant, D., & Gorenstein, P. 1983, *ApJ*, 267, 535  
 Feigelson, E., Wood, P., Schreier, E., Harris, D., & Reid, M. 1987, *ApJ*, 312, 101  
 Finoguenov, A., & Jones, C. 2001, *ApJ*, 547, L107  
 Ford, H., et al. 1994, *ApJ*, 435, L27  
 Forman, W., Jones, C., & Tucker, W. 1985, *ApJ*, 293, 102  
 Gavazzi, G., Boselli, A., Vilchez, J. M., Iglesias-Paramo, J., & Bonfanti, C. 2000, *A&A*, 361, 1  
 Harms, R. J., et al. 1994, *ApJ*, 435, L35  
 Harris, D., Biretta, J., & Junor, W. 1999a, in *The Radio Galaxy Messier 87*, ed. H.-J. Roser & K. Meisenheimer (New York: Springer), 100  
 Harris, D., Biretta, J., Junor, W., Perlman, E., Sparks, W., & Wilson, A. 2003, *ApJ*, 586, L41  
 Harris, D. E., Owen, F. N., Biretta, J. A., & Junor, W. 1999b, in *Diffuse Thermal and Relativistic Plasma in Galaxy Clusters*, ed. H. Böhringer et al. (MPE Rep. 271; Garching: MPE), 111  
 Heinz, S., Reynolds, C., & Begelman, M. 1998, *ApJ*, 501, 126  
 Hines, D., Owen, F., & Eilek, J. 1989, *ApJ*, 347, 713  
 Jordan, A., et al. 2004, *ApJ*, 613, 279  
 Kaiser, C. 2003, *MNRAS*, 343, 1319  
 Kaiser, C., & Binney, J. 2003, *MNRAS*, 338, 837  
 Kraft, R., et al. 2003, *ApJ*, 592, 129  
 Lumb, D., Warwick, R., Page, M., & De Luca, A. 2002, *A&A*, 389, 93  
 Macchetto, F., Marconi, A., Axon, D. J., Capetti, A., Sparks, W., & Crane, P. 1997, *ApJ*, 489, 579  
 Marshall, H., Miller, B., Davis, D., Perlman, E., Wise, M., Canizares, C., & Harris, D. 2002, *ApJ*, 564, 683  
 Mathews, W. 1978, *ApJ*, 219, 213  
 Matsushita, K., Belsole, E., Finoguenov, A., & Böhringer, H. 2002, *A&A*, 386, 77  
 McNamara, B. R., et al. 2000, *ApJ*, 534, L135  
 Molendi, S. 2002, *ApJ*, 580, 815  
 Nulsen, P., & Böhringer, H. 1995, *MNRAS*, 274, 1093  
 Nulsen, P., David, L., McNamara, B., Jones, C., & Forman, W. 2002, *ApJ*, 568, 163  
 Owen, F., Eilek, J., & Kassim, N. 2000, *ApJ*, 543, 611  
 Perlman, E. S., Biretta, J. A., Sparks, W. B., Macchetto, F. D., & Leahy, J. P. 2001, *ApJ*, 551, 206  
 Peterson, J., et al. 2003, in *The Riddle of Cooling Flows in Galaxies and Clusters of Galaxies*, ed. T. H. Reiprich et al. (Charlottesville: Univ. Virginia), <http://www.astro.virginia.edu/coolflow/proc.php>  
 Reynolds, C., Heinz, S., & Begelman, M. 2001, *ApJ*, 549, L179  
 Ruszkowski, M., Bruggen, M., & Begelman, M. 2004, *ApJ*, 611, 158  
 Sparks, W. B., Biretta, J. A., & Macchetto, F. 1996, *ApJ*, 473, 254  
 Sparks, W., Donahue, M., Jordan, A., Ferrarese, L., & Côte, P. 2004, *ApJ*, 607, 294  
 Stewart, G., Fabian, A., Nulsen, P., & Canizares, C. 1984, *ApJ*, 278, 536  
 Tabor, G., & Binney, J. 1993, *MNRAS*, 263, 323  
 Tonry, J., et al. 2001, *ApJ*, 546, 681  
 van den Bergh, S., McClure, R., & Evans, R. 1987, *ApJ*, 323, 44  
 Young, A., Wilson, A., & Mundell, C. 2002, *ApJ*, 579, 560